TEKTONIKA

What Can GNSS Tell About Physical Processes in Slowly Deforming France? Insights From a Community Benchmark Exercise

Marianne Métois [*1], **Stéphane Mazzotti** [2], **Axel Periollat** [3], **Adrien Damon** [3], **Juliette Grosset** [3], **Frédéric Masson** [4], **Marguerite Mathey** [5], **Jesús Piña-Valdés** [6], **Alexis Rigo** [7], **Anne Socquet** [8], **Taku Ueda** [9], **Mathilde Vergnolle** [10], **Philippe Vernant** [3]

[1]Université Claude Bernard Lyon 1, ENS de Lyon, Université Jean Monnet, CNRS, LGL-TPE, UMR5276, Lyon, France | [2]Laboratoire de Planétologie et Géosciences, Nantes Université, CNRS, Nantes, France | [3]Géosciences Montpellier, Université de Montpellier, CNRS, Montpellier, France | [4]Institut Terre et Environnement de Strasbourg (ITES) UMR 7063, Université de Strasbourg, CNRS, Strasbourg, France | [5]Autorité de Radioprotection et de Sureté Nucléaire (ASNR), PSE-ENV/SCAN/BERSSIN, F-92260, Fontenay aux Roses, France | [6]Departamento de Ciencias Geodésicas y Geomática, Escuela de Ciencias y Tecnología, Universidad de Concepción Campus, Los Ángeles, Chile | [7]Laboratoire de Géologie, CNRS, École Normale Supérieure, PSL University, Paris, France | [8]ISTerre, Université Grenoble Alpes, Université Savoie Mont Blanc, CNRS, IRD, Grenoble, France | [9]National Research Institute for Earth Science and Disaster Resilience, 3-1 Tennodai, Tsukuba-shi, Ibaraki, 305-0006, Japan | [10]Observatoire de la Côte d'Azur, Université Côte d'Azur, CNRS, IRD, Géoazur, 250 rue Albert Einstein, Sophia Antipolis 06560 Valbonne, France

Abstract Analysis of crustal deformation is key to understand current tectonics, deformation processes and seismicity. However, there is no consensus to date on how to integrate geodetic strain rates in seismic hazard models for continental intraplate regions. Most of Western Europe and mainland France are located within the Eurasia Plate, with very low deformation and seismicity rates, and GNSS velocities that comprise different sources, from tectonic contributions (e.g., fault motions) to non-tectonic long-term or transient processes (e.g., Glacial Isostatic Adjustment - GIA). Some of these processes also reflect stress changes at depth, loading of active faults, and seismicity. Understanding this deformation is therefore key to better assess seismic hazard in slow straining areas. In order (i) to assess the variability due to the diversity of strain-rate calculation methods and (ii) to test their capacity to resolve low-amplitude deformation, we conduct a benchmark exercise based on synthetic velocity fields comprising background noise (with the same characteristics as that observed in mainland France) plus velocity signals from various geodynamic processes. Comparing to the expected values the strain rates derived independently by eight different methods, four main conclusions can be drawn. (1) The capacity to deal with velocity noise and recover large-scale or local signals vary strongly between the methods, with some standing out from the others. (2) No method is able to retrieve the strain rate signals associated with active faults slipping at rates of 0.3-1 mm/yr (i.e. larger than expected for mainland France). (3) No method is able to retrieve the small deformation associated with a potential hot spot under the Massif Central (similar to, but about twice lower than observed for the Eifel hotspot). (4) Some methods are able to retrieve parts of the large-scale strain rate patterns (but not the amplitudes in general) associated with Alpine GIA or rotating rigid blocks. These results must be interpreted with caution, keeping in mind the strict benchmark design. They point out the potential for improvements in future analyses of geodetic deformation in mainland France and continental intraplate context in general.

Executive Editor:
Robin Lacassin
Associate Editor:
Devin McPhillips
Technical Editor:
Mohamed Gouiza

Reviewers:
Kathryn Materna
Corné Kreemer

Submitted:
2 December 2025
Accepted:
30 March 2026
Published:
24 April 2026

1 Introduction

Rather than looking at (messy) velocity fields derived from GNSS time series and representing either long-term velocities or abrupt displacements, deriving continuous maps of strain rates is more and more often considered. This method offers an alternative view to the deformation characteristics that gets rid of reference-frame related issues and allows for a more direct and straightforward comparison with other geological or geophysical observations (earthquakes, fault traces, stress measurements, etc). The tendency is to get more data to provide estimates of long-term velocities: denser GNSS-derived velocity fields of varying quality (e.g., campaign mode, low-cost, RTK), velocity fields from InSAR time series at regional to continental scales (e.g. *Wang and Wright*, 2012; *Ou et al.*, 2022; *Lemrabet et al.*, 2023; *Elliott et al.*, 2026), displacement fields from optical correlation (e.g. *Barnhart et al.*, 2020;

*✉ marianne.metois@univ-lyon1.fr

Cheng and Barnhart, 2021; *Antoine et al.*, 2021; *Li et al.*, 2023), etc. Strain rate maps derived from these data sets (alone or in combination) are now calculated routinely and used for tectonic interpretation. However, these calculations are not straightforward, in particular when looking at very low strain rates.

Being more commonly produced and published, maps of strain rates are also more often integrated in seismic hazard calculations (*Beauval et al.*, 2018; *Meletti et al.*, 2021; *Donniol Jouve et al.*, 2024). One way of doing so consists in integrating seismic hazard models constrained only by geodetic data in PSHA calculations, with Gutenberg-Richter laws derived from Kostrov calculations of geodetic moment rates (*Ward*, 1998; *Jenny et al.*, 2004; *Mazzotti et al.*, 2011; *D'Agostino*, 2014). Other approaches propose to take into account geodetic constraints more indirectly, for example to refine seismic zoning and local tectonic style, or combined with geological observations in consistent models (*Petersen et al.*, 2024; *Pollitz et al.*, 2022). To date, no consensus exists on the best way to integrate these constraints in robust seismic hazard estimates, and information coming from geodesy is still associated with relatively low weights in hazard logic trees (e.g. *Meletti et al.*, 2021; *Petersen et al.*, 2024), when considered at all. This may come from the legitimate distrust of strain rate calculations that are prone to interpolation artifacts that limit their interpretations (*Baxter et al.*, 2011), and also to the discrepancy between seismic potential derived from geodesy and from seismology in some regions (e.g. *Jouve et al.*, 2024).

In mainland France, where strain and seismic rates are very low, it is still unclear how geodesy can help improve seismic hazard models. Recent significant earthquakes (Mw=5, 2019, Le Teil; Mw=5, 2023, La Laigne, or Mw=3.9, 2019, Jonzac) are in relative agreement with the geodetic strain rate principal directions and tectonic styles (*Masson et al.*, 2019a; *Cornou et al.*, 2020). However, part of the current surface deformation may not be representative of the crustal state of stress (*Grosset et al.*, 2023), reflecting the potential stress / strain disagreement associated with short-term GNSS data (*Wang*, 2000; *Townend and Zoback*, 2006). A first step in integrating geodesy in seismic hazard models in France is to build maps of geodetic strain rate as reliable as possible and associated with robust uncertainties. This is what is expected in the framework of the Alceste project piloted by academic researchers at the request of the French Ministry of Ecological Transition in charge of risk management, which should provide a new hazard map by 2026.

In this study, we present results from the first contribution to this major work by the scientific community involved in the national observing service RENAG (*RESIF*, 2017). We have focused our efforts on understanding our collective ability to retrieve expected geodynamic signals from the computation of strain rate maps from GNSS velocity fields. In the following, we present the design and results of a benchmark exercise in which we test the ability of several methods used in the French and international community to compute strain rates from synthetic velocity fields covering mainland France.

2 Rules of the Game

2.1 Design of the Benchmark Exercise

This study aims at assessing which geodynamic signals may be retrieved by different strain-rate methods over mainland France. To do so, we have designed a benchmark exercise, or data challenge, inspired from the pioneer work of *Sandwell et al.* (2010) in California, that proposes to test the ability of each participant's method to retrieve strain rate characteristics expected from synthetic velocity fields, i.e. properly retrieve its spatial derivatives. Given the intraplate context of mainland France and its low level of seismic activity, we built synthetic velocity fields (hereafter called "models") that reflect a realistic level of noise and surface deformation coming from active faults (either creeping or locked), rigid block rotations, but also from non-tectonic transient motions associated with Glacial Isostatic Adjustment (GIA) due to the melting of the Alpine Würm ice sheet, or flexure associated with supposed hotspot activity in the Massif Central.

Eleven models were produced and made accessible to the participants (hereafter referred to as "players"). Each player was provided with (i) some knowledge of the kind of geodynamic signal included in the models and (ii) cleaned velocity fields to be used for their calculation. To do so, velocity outliers were detected and removed based on "interquartile range" statistics at a regional scale (i.e., considering clusters of about 200 km radius).

This study has not been designed for systematic comparison between the techniques/codes used by each player (detailed in the following section). Many parameters come into play when computing strain rates from a velocity field, including subjective choices of the user that may vary depending on its a priori knowledge of the data structure and noise, such as the choice of smoothing parameters. The geodynamic signals expected in mainland France come from very different physical processes producing variable deformation patterns in both amplitude and wavelength. Therefore, the parameterization used in each method could differ depending on the synthetic model considered, making the task of comparing the different results nearly impossible. Thus, in this exercise, the players had to choose a single parameterization for their method, which they kept constant for computing strain rates from all 11 synthetic velocity fields. Further discussion on this constraint is provided in section 5.

Computing the strain rate tensors from discrete velocities is a highly non-unique problem, and most methods (but not all) developed to do so first interpolate the velocity field before taking its derivatives. They therefore provide predicted velocities at observation points, allowing estimations of data fit that are usually very good (few tenth of mm/yr on average). However, because the goodness of the data fit is a necessary but

not sufficient condition to recover the correct strain rate pattern, we do not compare directly observed and predicted velocities in this exercise, but rather focus on estimating indicators derived from velocity gradients (see section 2.3).

2.2 Strain Rate Analysis Methods

Table 1 summarizes the 8 different methods that have been tested, applied by 7 different players coming mostly from the scientific community involved in the french national observation service RENAG (https://renag.epos-france.fr). In the following, in order to ease the reading, we refer to each method with a letter (A to H) and describe the parameterization choices.

Table 1 – Methods used in the benchmark exercise, * refers to methods using explicitly vertical velocities.

Code	Method
A*	Geostrain (*Goudarzi et al.*, 2015)
B	VISR3D (*Piña-Valdés et al.*, 2022), modified from *Shen et al.* (2015)
C	StrainTool (*Anastasiou et al.*, 2019), based on *Shen et al.* (2015)
D	SPARSE (*Haines and Holt*, 1993), modified from *Kreemer et al.* (2000)
E*	Gaussian smoothing (*Mazzotti et al.*, 2011; *Masson et al.*, 2019a)
F	B-Strain (*Pagani et al.*, 2021)
G	STIB (*Masson et al.*, 2014)
H	Basis function expansion (BSF, *Okazaki et al.*, 2021)

A: Geostrain is a Least Square Collocation (LSC) method developed on a spherical Earth and described in details in *Goudarzi et al.* (2015). Geostrain is used with a Gaussian correlation function and a correlation distance of 175 km. Strain rates calculations take into account the vertical velocities as in **E** (*Mazzotti et al.*, 2011).

B: The VISR3D method comes from the initial method of *Shen et al.* (2015) that has been slightly modified by *Piña-Valdés et al.* (2022). The velocity field is used to invert for strain rate tensors using the VISR technique from *Shen et al.* (2015) adapted for cartesian coordinates. The weighting threshold parameter W_t is set at 48. VISR3D method implicitly assumes a spatially variable smoothing parameter: the higher W_t, the smoothest the solution.

C: StrainTool (*Anastasiou et al.*, 2019) is an open source python suite https://github.com/DSOlab/StrainTool based on the VISR method of *Shen et al.* (2015) and used by the EPOS-GNSS consortium to provide their strain-rate product (*Fernandes et al.*, 2022). It has been used by the player with the default set of parameters, i.e. W_t set to 24 and the optimal smoothing distance chosen by exploring the 1-500 km interval by steps of 1 km. Since Straintool does not allow for station duplicates, when two velocities are available for the same site, the velocity with the higher uncertainty is discarded.

D: The SPARSE code developed by *Haines and Holt* (1993) derives strain rates from the horizontal velocities that are interpolated using a bi-cubic Bessel spline technique (*Beavan and Haines*, 2001). The lithosphere is supposed to be homogeneous, with a single smoothing parameter (sm 0.25) used over the whole region.

E: The Gaussian smoothing method relies on computing at each grid node the 3D velocity and the horizontal strain rate tensor by weighting the observed 3D velocities by a Gaussian function of the distance between the computation point and the GNSS site, and the inverse of the velocity uncertainty. Uncertainties lower than 0.01 mm/yr are set to 0.01 mm/yr. In this method, the vertical component of the velocity is used for the computation of the horizontal strain rate by assuming a radial motion on a sphere, i.e.: isotropic extension rate $= \frac{V_{up}}{R_{Earth}}$ (see *Mazzotti et al.*, 2011; *Masson et al.*, 2019a, for a full description).

F: The BStrain method inverts for the interpolated horizontal velocity field and strain rate tensors by using a bayesian transdimensional inversion (*Pagani et al.*, 2021; *Métois et al.*, 2025). As for method E, uncertainties lower than 0.01 mm/yr are set to 0.01 mm/yr. The same a-priori conditions and convergence parameters are used for all the models, and 1 million of iterations are considered. To compare with the results from other players, we plot the median of the probability density functions (PDF) associated with each component of the interpolated strain rates. Where the standard deviation of the interpolated horizontal velocity PDF is higher than 2 mm/yr, results are disregarded and not plotted.

G: The STIB method (*Masson et al.*, 2014) is used with a smoothing parameter chosen to be 200 and a damping factor of 10^{-9}. This inversion technique is inspired from the delay-time seismic tomography considering temporal variations of the baseline lengths all over the study area.

H: Horizontal interpolated velocities and 2D strain rates are computed using the basis function expansion (BSF) method (*Okazaki et al.*, 2021; *Okazaki*, 2025). Basis functions are placed with 30 km intervals. The hyper parameter is objectively determined by minimizing ABIC, so spatial smoothness depends on the model. The velocity uncertainties are not taken into account in the computation.

Two contributions are proposed using codes derived from the same VISR method developed by *Shen et al.* (2015) (**B, C**). Others are proposed by players who have developed their own method and have therefore a high level of expertise for this specific method (**E, F, G**), while others are end users (**A, C, D, H**).

2.3 Conventions and Format

We ask all players to provide their results on a 0.5°×0.5° grid, for each synthetic velocity field. The file structure is described in supplementary table S1, note that we define the second invariant I_2 as $\sqrt{\dot{\epsilon}_{xx}^2 + \dot{\epsilon}_{yy}^2 + 2\dot{\epsilon}_{xy}^2}$; and the divergence d as $\dot{\epsilon_{xx}} + \dot{\epsilon_{yy}}$. Some codes do not allow for simple control on the grid output and impose, for instance, a regular grid in Cartesian coordinates that slightly differs from our reference grid. In this case (**C**), we interpolate linearly and resample the results. Contribution **D** gives angular vorticity in °/Myr that we convert in /yr assuming $\omega = f \times \omega_{ang}$ with $f = 2\pi/(180 \times 10^6)$.

3 Building Synthetic Velocity Fields

3.1 GNSS Network in Mainland France

Mainland France is quite densely covered with GNSS permanent stations from academic, public, and private networks producing position time series of heterogeneous quality and duration (Figure 1). However, because of the large number of potentially active faults and their very low loading rates (lower than 1 mm/yr, *Jomard et al.*, 2017), this coverage may be too sparse to capture the deformation associated with single features. Therefore, since the 2000s, the academic community has developed and maintained complementary networks of benchmarks particularly dense in tectonically active zones (Alps, Pyrenees, southeastern France), which positions are measured on an episodic basis.

Several secular velocity fields have been computed and published in recent years, encompassing subsets of these potentially available observations (*Déprez et al.*, 2018; *Masson et al.*, 2019a; *Piña-Valdés et al.*, 2022; *Santamaría*, 2022). In our theoretical exercise, we aim at exploring what kind of deformation signal (shape and amplitude) is reasonably detectable using GNSS long-term velocities. We therefore chose to sample our synthetic velocity fields on a reasonably optimistic available network, i.e., we associate a velocity value to each GNSS station in mainland France that has already been used to build these secular velocity fields, whether the station is still operating or not, and including all known benchmark networks (hereafter called semi-permanent). We did not include stations from the recent Centipede network (*Bosser et al.*, 2024; *Ancelin et al.*, 2025), since it remains unclear up to now whether we can use these stations to derive robust long-term velocities. Added to permanent stations from other networks abroad, that have not been considered exhaustively, this results in a theoretical network composed of 1600 stations covering France and neighboring countries.

The density of stations in our idealized network is highly variable: the highest densities are observed in the Paris basin that benefits from a large number of private GNSS stations distributed via the RGP network, together with the Pyrenees and the Alps where the existing academic stations are complemented by semi-permanent networks. Fewer stations operate in Massif Central and western France. To further explore the impact of the network design on our results, we consider four boxes of about 150 000 km^2 (Figure 1): (1) the Alps and Rhone Valley, (2) the Pyrenees, (3) the Armorican Massif and western Massif Central, and (4) the Paris Basin. We use the same idealized network to build 11 distinct synthetic velocity fields, or "models", as listed in Table 2 and presented in the following sections. The synthetic horizontal and vertical velocity fields from these models are presented in Figure 2 and Figure S5 (Supporting Information), without adding the reference noise model, to better show the expected geodynamic signal. For each synthetic model, we compute the theoretical strain rates indicators on a 0.5° grid: principal strain rates directions, I_2, divergence and vorticity, all presented in Figures S2 to S4 in Supporting Information. For all models except 7 and 11 (i.e., block rotation models), the theoretical strain rate tensors are computed at each grid node based on analytical formulations from elastic plate flexure and fault dislocation equations. We compute vorticity from a dense and regular 0.1° x 0.1° velocity field using standard gradient computation in order to minimize interpolation artifacts. The same strategy is used to compute the strain rate tensors and their invariants for velocity fields computed using rigid blocks. Vorticity is computed analytically for model 7 (rigid blocks and noise).

3.2 Building Noise Models [1, 2, 3]

In order to test the sensitivity of the methods to the noise content, we generate three synthetic velocity fields containing only noise, i.e., free from any coherent geodetic and geodynamic signal. Since the spatial structure and frequency content of noise in GNSS time series is still a research issue (*Benoist et al.*, 2020; *Costantino et al.*, 2023; *Gobron et al.*, 2024; *Rebischung and Gobron*, 2024), generating realistic noise models associated with velocity fields is not trivial. Our velocity noise models are based on randomly selected synthetic velocities from *Masson et al.* (2019b), with minor adjustments to the statistical properties to ensure noise characteristics that correspond to the mainland France observations. These velocities are derived from synthetic position time series of durations of 3–21 years, with colored noise amplitudes of 0.6–4.4 mm and spectral indices of -0.9 to -0.01, and with a number of offsets that depend on the series' length. Details of the synthetic velocity creations can be found in *Masson et al.* (2019b) and in Figure S1 (Supporting Information) and Data Availability section.

The statistical characteristics of the noise-model velocities are given in supplementary material, compared to those of actual velocities in mainland France from (*Masson et al.*, 2019b; *Piña-Valdés et al.*, 2022; *Grosset et al.*, 2023). In summary, the interquartile ranges of our synthetic horizontal and vertical velocities are 0.1–0.15 mm/yr and 0.3 mm/yr, respectively, compared to 0.3–0.4 mm/yr and 0.7–0.8 mm/yr for the observed velocity solutions. Thus, our synthetic noise-model

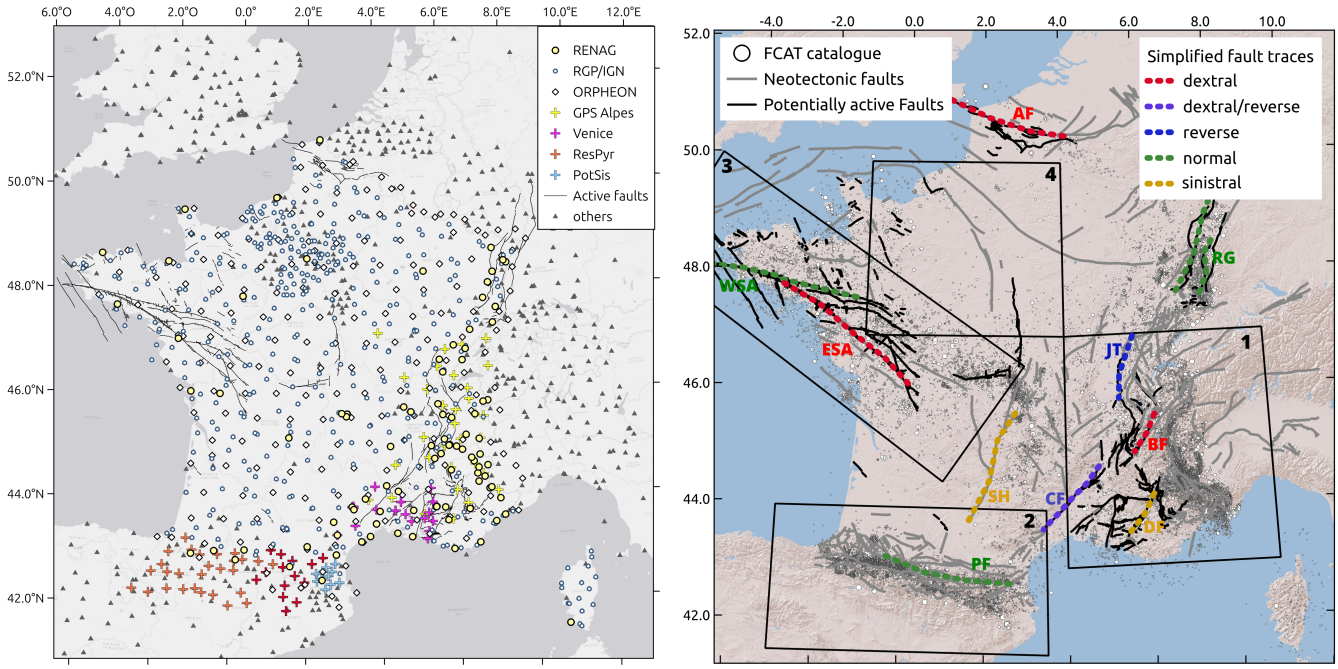

Figure 1 – Left: GNSS networks available and used in our study area. Continuous academic (*RESIF*, 2017) or non academic networks (RGP https://rgp.ign.fr/ and Geodata-Orpheon data archived at *re3data.org*, 2022) are plotted as circles and diamonds. Semi-permanent or campaign mode benchmarks networks installed in the most tectonically active area are plotted as colored crosses: Venice (*Masson et al.*, 2003), ResPyr (*Chenel et al.*, 2009; *Rigo et al.*, 2015) , PotSis (*Talaya et al.*, 1999), GPS Alpes (*Vigny et al.*, 2002; *Walpersdorf et al.*, 2018). Gray triangles are stations from other networks with published velocity that we use to build our synthetic velocity field. Active faults are from *Jomard et al.* (2017). Right: Earthquakes from the FCAT catalogue (*Manchuel et al.*, 2018) as circles that scale with magnitude. Simplified traces of major faults used to build synthetic models 4 to 7 are shown as dotted colored segments. ESA - Eastern South Armorican Fault; BF - Belledonne Fault; AF - Ardenne Front; RG - Rhine Graben; PF - Pyrenean Front; WSA - Western South Armorican Fault; JT - Jura Thrust; CF - Cevennes Fault; DF - Durance Fault; SH - Sillon Houiller. Black boxes correspond to four subzones. 1- Alpine area, 2- Pyrenean area, 3- Armorican and western Massif Central, 4- Paris Basin.

Table 2 – 11 synthetic velocity fields: number, content, and description.

Model	Content	Details
1	Noise 1	Same as Noise 3 but with half amplitude
2	Noise 2	Same amplitude as Noise 3 but spatially different
3	Noise 3	Reference noise
4	Creeping no noise	Active faults creeping at 0.3 mm/yr, no noise added
5	Creeping + noise	Active faults creeping at 1 mm/yr, noise added
6	Locked + noise	Locked faults at rates 1mm/yr, noise added
7	Blocks + noise	Rigid block rotations, noise added
8	GIA Alps + noise	Visco-elastic rebound expected from Glacial Isostatic Adjustment associated with the Alpine ice sheet melting, noise added
9	MC hot spot + noise	Surface flexure modeled for a theoretical hot spot under Massif Central, noise added
10	Locked + GIA + MC + noise	Combination of models 6, 8 and 9, noise added
11	Blocks + GIA + MC + noise	Combination of models 7, 8 and 9, noise added

velocities show a smaller dispersion (by a factor of ∼2), which can be attributed to the fact that the actual velocities contain tectonic or solid Earth signals of amplitudes ca. 0.1–1 mm/yr (e.g., deformation in the Alps and Pyrenees). Alternatively, the lower dispersion of our synthetic data sets may indicate that our noise model is slightly optimistic, which will be taken into account in the analyses and discussions of the results. The velocity uncertainties in our synthetic noise model are characterized by median values of 0.15 mm/yr and 0.4 mm/yr for the horizontal and vertical components, respectively, and a correlation coefficient with the velocities of 0.3–0.5. These synthetic uncertainty statistics are similar to those of actual velocity solutions.

Hereafter, the three noise models are referred to as model 1, 2, and 3 (Table 2). Models 2 and 3 have the same statistical properties but with two different random

samplings of velocities at the GNSS stations, allowing us to test the effect of the regional station distribution as a function of noise location. The first model (model 1) corresponds to model 3, with velocities and uncertainties divided by two. Model 3 also serves as the reference noise model that is added to the tectonic models defined below. By definition, the "true" strain rate invariants and vorticity associated with these models are null.

3.3 Fault and Tectonic Models [4, 5, 6, 7]

In mainland France, rates of potentially active faults barely reach 0.1 mm/yr (*Jomard et al.*, 2017), i.e. very low slip rates. We chose to overestimate these slip rates up to 1 mm/yr in order to maximize the surface deformation that could be associated with active faults. We use a subset of faults from the database of potentially active faults (BDFA) in mainland France (*Jomard et al.*, 2017), selected to capture the variability in fault styles and locations: normal faulting in the Pyrenees, the Upper Rhine Graben, and the northern branch of the South Armorican Shear Zone, strike-slip faulting in the South Armorican Shear Zone, the Massif Central, the Western Alps, and the North-Artois Shear Zone, reverse faulting in the French Juras and the Cévennes (Figure 1-right). Each fault trace is simplified to a continuous segment with a single homogeneous dip. These simplifications likely impact near-field (< 10 km) velocities and strain rates, but they have very little to no effect at distances sampled by the GNSS network (few 10s km).

We create three sets of fault-related synthetic velocities where all faults have the same slip characteristics (Table 2 and Figure S2 in Supporting Information): model 4, in which all faults creep at a slip rate of 0.3 mm/yr; model 5, in which all faults creep at a slip rate of 1 mm/yr; model 6, in which all faults are locked (i.e., in the interseismic phase of strain accumulation) at 1 mm/yr. For the last two (models 5 and 6), we add random noise from our reference noise model (model 3). Model 4 remains noise free, thus allowing us to test a best-case scenario for potential faults with a reasonable slip rate in the context of mainland France, while the other two models allow testing the detection capacity for unreasonably fast faults, but with a reasonable noise level.

Fault-related velocities are computed using formulations for dislocations in an elastic half-space (*Okada*, 1985), with slip dislocations between 0 and 15 km depth for the creeping-fault models (models 4 and 5) or between 15 and 100 km depth for the locked-fault model (model 6). The fault traces are independent and not connected, resulting in the main deformation patterns concentrated within ∼100 km of the fault traces (Figure 2). This unusual model is meant to replicate very slow unconnected faults loaded by far-field stresses without large-scale tectonics, as expected in intraplate contexts.

A second set of models is created to represent potential rigid block rotations in mainland France and nearby areas. The block boundaries are chosen to reflect large crustal-scale structures, most of which are similar to the fault traces used in the fault models, while others are only there to "close" the blocks outside of our area of interest (Figure S3, Supporting Information). Relative block rotations, i.e., relative to overall France, are defined to reproduce the first-order patterns observed in the GNSS velocity solution of (*Masson et al.*, 2019a). The rotations characteristics are given in supplementary table S2. This block model provides an alternative "plate boundary tectonics" version to the fault model, in which all faults are connected in a consistent kinematic framework where the block-boundary faults are creeping at slip rates imposed by the relative block motions. The main block model (model 7) comprises only the rigid-block velocities combined with the reference noise model (model 3). Block boundaries are vertical creeping faults, resulting in large values of divergence and I_2 in the vicinity of the boundaries only. Inside each block, the divergence and second invariant are expected to be zero, while the vorticity is uniform (Figure S3, Supporting Information).

3.4 Flexure Models [8, 9]

The last set of geodynamic models represents the flexural response of the lithosphere to both external and internal processes (Table 2; Figure S4 in Supporting Information): Model 8 corresponds to present-day Glacial Isostatic Adjustment in response to the loading of the lithosphere by the Pleistocene (Würm) alpine glaciers and ice sheets (e.g. *Walpersdorf et al.*, 2018; *Sternai et al.*, 2019; *Grosset et al.*, 2023). The ice loading model is based on the glacier reconstruction at the Last Glacial Maximum (LGM, ca. 21 ka BP) by *Mey et al.* (2016). The model covers the entire Alps, with ice thicknesses up to 2000–2500 m in the deepest valleys. The response of the lithosphere is computed with the open-source gFlex code (*Wickert*, 2016) assuming a simple elastic plate overlying a Newtonian viscous fluid (i.e., 1D Maxwell rheology), with an elastic plate thickness of 60 km and a viscous relaxation time of 5500 yr, following *Grosset et al.* (2023) and *Damon et al.* (2023). Ice-sheet melting is supposed to occur instantaneously at 17 ka (*Seguinot et al.*, 2018). The predicted horizontal velocity field (Figure 2) shows a standard radial outward pattern associated with upward flexure of the alpine region, with horizontal and vertical velocities up to ∼0.5 mm/a and ∼1.5 mm/a, respectively.

Model 9 is created to represent the potential effect of a hotspot underneath the Massif Central. The lithosphere response to such an upper mantle dynamics is modeled as the flexure of a 20 km-thick elastic plate, using the gFlex software, driven by an upward push centered under the Massif Central (diameter of the plume circa 80 km). The response is then scaled to fit the GNSS velocities observed in Belgium and Germany, proposed to represent deformation due to the hotspot associated with the Eifel Volcanic Field (*Kreemer et al.*, 2020). The predicted velocities are about twice smaller than those of the Alpine GIA model, with a circular pattern centered on the Mont Dore volcanic system (45.0827°N, 2.6836°E).

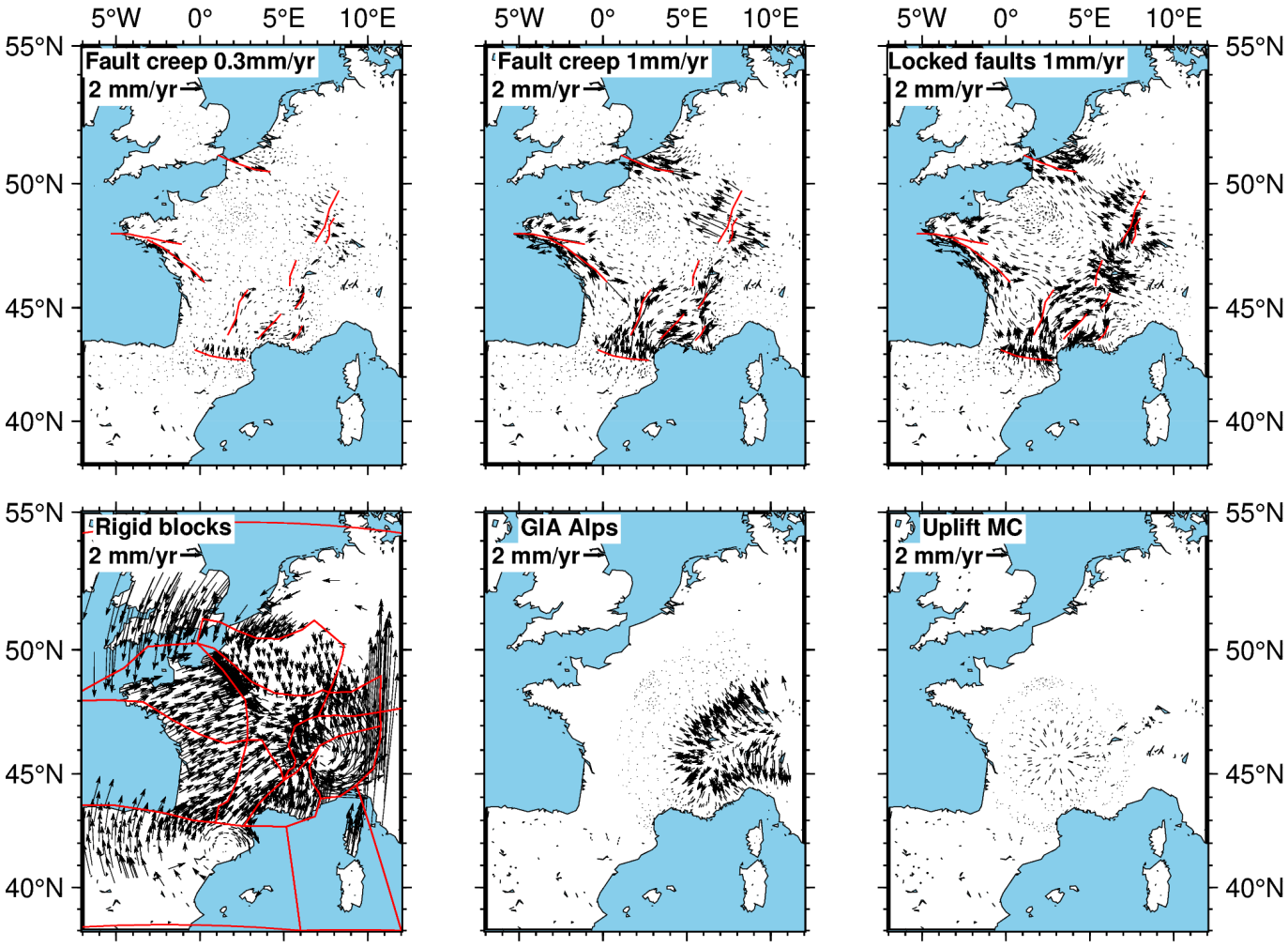

Figure 2 – Synthetic horizontal velocity fields computed based on geophysical assumptions and combined with noise to build models 4 to 9 (from left to right, top to bottom). Vertical velocity fields are provided in Figure S5 (Supporting Information).

For models 8 and 9, the theoretical vorticity is computed by derivation of the interpolated velocity field.

These two flexural models are combined and added to the 1 mm/yr locked-fault model (model 6) to produce model 10 (Alpine GIA + Massif Central hotspot + fast active faults). Model 11 includes both flexural models and block rotations as in model 7. Finally, all four models are combined with the reference noise model 3. Note that the theoretical strain rates invariant and vorticity are computed and not given analytically for these combined models.

4 Results

Results are summarized here as maps of second invariant I_2 (i.e., total strain), divergence (i.e., dilatation / contraction), vorticity (i.e., rotation), and principal directions retrieved by each player (Table 1) for each model (Table 2), with the full sets presented in Supporting Information (Figures S7 to S21). In each figure, we present the theoretical values (upper left panel) and what is effectively retrieved by the contributors, using the same color scale for comparison (see Figure 3 for instance). We quantify the agreement between the true value and the inverted ones using different metrics that give an overall idea of the performance of each method: we compute the RMS (root-mean-square) of the difference between the true and retrieved maps by summing residuals on each pixel (blue histograms in Figure 3) and the correlation between the true and retrieved maps (where the true value is not zero, i.e. models 4 to 11, black diamonds in Figure 3). We also compute an autocorrelation score (red triangles in Figure 5) in order to have an idea of how the results are controlled by noise. The autocorrelation score is obtained by computing the correlation between the results for the specific model and for the reference noise model 3. Thus, an autocorrelation score significantly lower than one indicates that the results are likely to be meaningful and contain signal that differs from noise.

4.1 Do We See Noise?

Some results for model 3 containing only noise are presented in Figure 3 (see Figures S7, S8 and S9 for complete results from all noise models). At first glance, we clearly see that some contributions deviate significantly from the expected null pattern regardless of the indicator considered. The residual RMS is always maximal for contributions C and G. We compute the wRMS between observed and predicted velocities for methods allowing this analysis, as shown in Figure S24

(Supporting Information). No significant overfitting is observed for method C, nor systematic misfit for methods A, F and H, that are considered to be performing slightly better than others. This confirms that the fit to the observed velocities is not efficient to discriminate between methods.

The dispersion around zero (i.e., around the true model) of each contribution is a measure of its capacity to deal with velocity noise in extracting strain rates. These dispersions are shown as boxplots in Figure S10 (Supporting Information). They are summarized in Figure 4 as the widths associated with 67% of the distributions (CI67), i.e., the 67^{th} percentile for the second invariant I_2 (positive values) or the difference between the 83.5^{th} and 16.5^{th} percentiles for the divergence and vorticity (negative and positive values). We compute these statistical indicators based on the entire study area in Figure 4, and on 4 geographic boxes presented in Figure 1 and in Figure S11 (Supporting Information). Overall, contributions A and H present the lowest dispersions around zero (i.e., the best capacity to deal with velocity noise), while contribution C shows the largest dispersion, about 100 times larger. The average 67% dispersions are about (0.1-1)$\times 10^{-9}$/yr. The dispersion is overall lower for all contributions in the Paris Basin where the station density is the highest, with only continuous GNSS stations. The results are closest to the true model for the noise model 1 in which the level of noise is half that in models 2 and 3 (Figure 4).

From this analysis, we can estimate confidence thresholds for each contribution, i.e., threshold values under which the contribution is unable to resolve actual signal from noise for I_2, divergence and vorticity. To do so, we compute the mean of these statistical indicators retrieved for the entire onshore part of models 2 and 3 and for their subsets as sampled by our 4 geographical boxes (Figure 1). Below these threshold values, as presented in Table 3, the results of the inversions should not be interpreted as actual signal and will be masked in the following. However, as discussed in the next section, some contributions that appear very resilient to noise (i.e., the threshold values are low for every indicator) nonetheless fail in retrieving geodynamic signal (see for instance contribution H). Contributions A, F, and H are the most resilient to noise, with low confidence threshold values, while contribution C is the most sensitive to noise. For models 4 to 11, we compute statistics (RMS, correlation and autocorrelation) based on pixels which value is above these confidence thresholds.

Table 3 – 67% confidence threshold values (in 10^{-9}/year) determined for each contribution and indicator, based on noise models 2 and 3 considered realistic. Q83.5 minus Q16.5 for the divergence and vorticity, Q67 for I_2, cf. text. Maximum thresholds for tuned methods are in bold, and can be considered as conservative values.

Contribution	Divergence threshold	I_2 threshold	ω threshold
A	0.069	0.09	0.033
B	**1.55**	**1.21**	0.34
C	3.46	4.18	1.5
D	0.28	0.33	0.13
E	0.82	0.71	**0.41**
F	0.06	0.17	0.011
G	1.22	1.03	0.36
H	0.01	0.02	0.0003

4.2 Do We See Geodynamic Signals?

4.2.1 Do We See Flexure?

We present retrieved maps of strain rates indicators for flexural models 8, 9 and 10 in supplementary Figures S12 to S15. We show on Figure 5, I_2 and divergence obtained for model 8 containing GIA signal and noise. Based on the noise analysis conducted in section 4.1, we choose to mask the areas where the retrieved values are lower than the confidence thresholds listed in Table 3. Results from contribution H are barely masked since the confidence threshold is very low, while large parts of the results from contributions B, C, D, E, and G are classified as non-interpretable (i.e., it is impossible to reconstruct the expected shape associated with the GIA signal from masked contributions B and E, for example). Unmasked maps are provided in Figure S23 (Supporting Information).

For model 9 containing a subtle flexure of the Massif Central due to a potential hotspot, autocorrelation scores are close to 1 (i.e., full correlation with reference noise model 3) for all strain rate indicators (Figures S12 to S15). We conclude that this geodynamic signal is invisible within the noise model, too small to be correctly recovered.

On the contrary, autocorrelations are lower than 1 for several contributions when retrieving strain rates for the Alpine GIA model (model 8). This is particularly notable for I_2 and divergence (Figure 5), for which the contributions A, F and H differ significantly from the reference noise model (A and F only when considering vorticity, see Figure S14 in Supporting Information). Significant correlations ($\geq$ 70%) with the expected I_2 are observed for contributions A, F and H, while good correlation scores are observed for divergence for contributions A and F, and for strain style patterns for contributions F and H (Figure S23, Supporting Information). These methods capture the alternation between the GIA inner extension and its compressive forebulge, retrieving the shape (and in amplitude for method F) of this pattern. The subtle change in vorticity ($\leq$ 0.5 nstrain/yr) induced by this GIA model is not convincingly retrieved by any method.

Figure 6 allows comparison of unmasked results of model 8 (Alpine GIA) along a NW-SE profile crossing the Western Alps. It underlines that contributions A and H that manage to recover a consistent signal in the divergence both underestimate it by more than 1 nstrain/yr at its maximum. Contribution F retrieves correctly the amplitude and overall shape of the northern

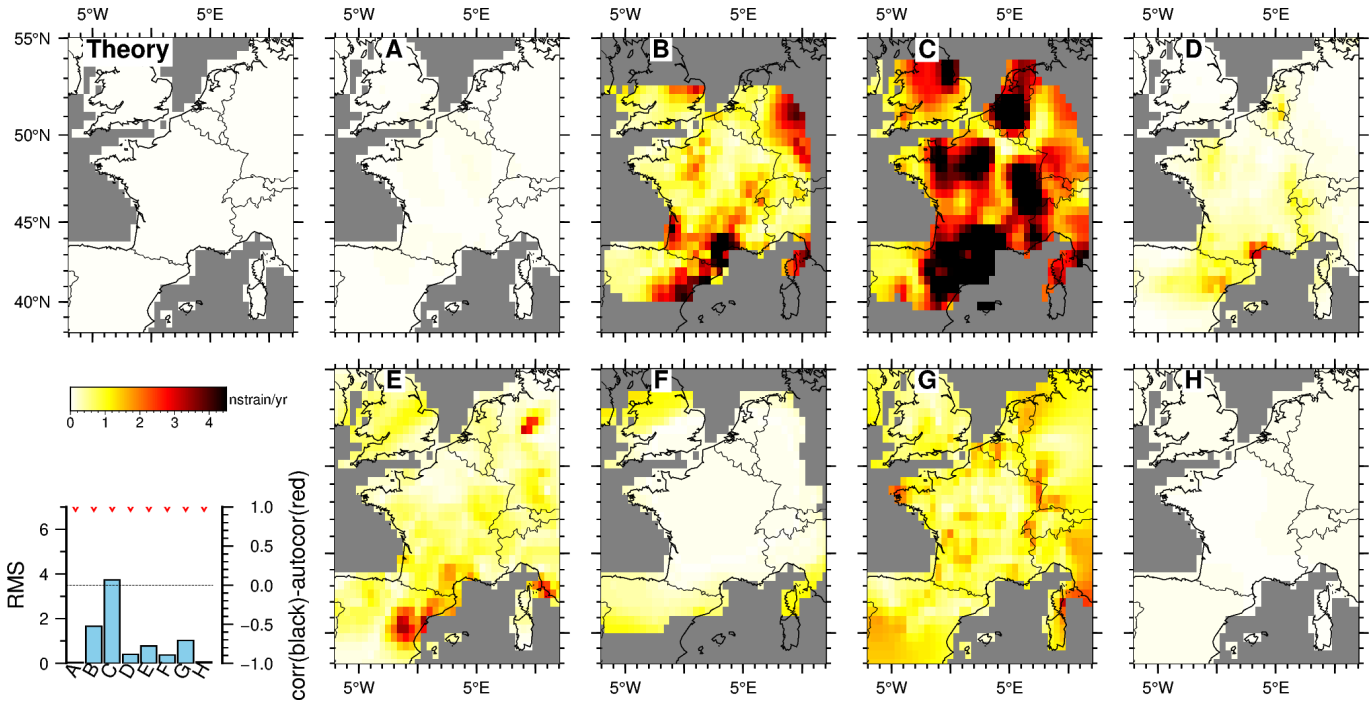

Figure 3 – Maps of retrieved I_2 for our reference noise model 3 and the 8 contributions (A to H, see Table 1). Gray area are where strain rates are not computed or considered unreliable (i.e. offshore). Lower left graph shows RMS as blue histogram.

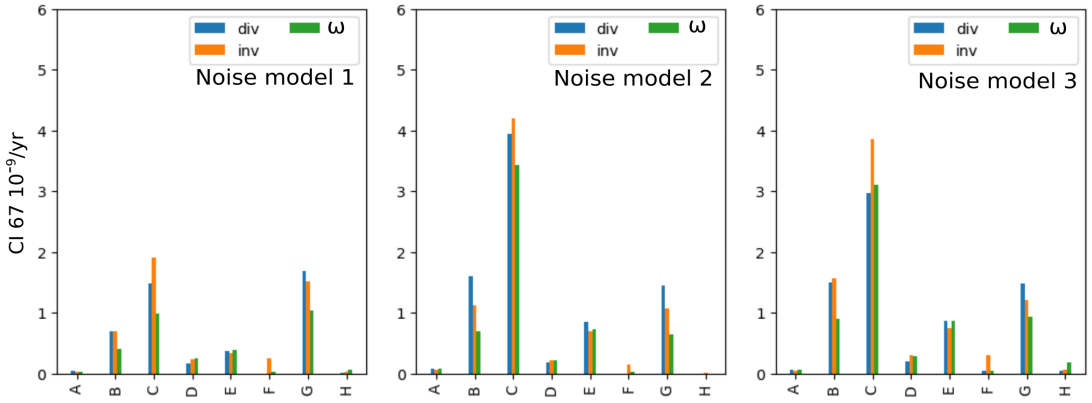

Figure 4 – Widths associated with 67% of the distributions (CI67), i.e., the 67^{th} percentile for the second invariant I_2 (positive values) or the difference between the 83.5^{th} and 16.5^{th} percentiles for the divergence and vorticity (negative and positive values) for the entire noise models 1, 2 and 3, from left to right.

part of the extension area, but fails in recovering its decrease to the south.

4.2.2 Do We See Active Faults?

We present retrieved maps of strain rates indicators for active faults models 4, 5 and 6 in supplementary Figures S17 to S19. In the main text, we show on Figure 7 results of the inversion of I_2 for these models. As for flexural models, we mask the results based on the confidence threshold determined for each contribution. However, we show the entire results for model 4 that is free of noise and contains only very small signal (creeping faults at 0.3 mm/yr).

In the peculiar case of this model 4, which is free of noise, 6 of the 8 contributions exhibit a significant correlation with the expected I_2 pattern, with a correlation score higher than 80% for contribution H (Figure 7). The very low correlation score for contribution F is probably due to outliers at the model boundaries. Results are significantly worse when looking at retrieved patterns of divergence and vorticity (supplementary Figures S17 and S18), for which only contribution H performs correctly (i.e. correlation higher than 50%). The tectonic style associated with each active structure is correctly recovered by contributions G and H (Figure S19, Supporting Information). Therefore, even in the absence of noise associated with surface velocities, it is very challenging to recover the strain rate signal of faults creeping at 0.3 mm/yr, while this rate is already too large for mainland France. I_2 is probably the most reliable and stable indicator to look for active faults in this case. Note that most methods are designed for continuous velocity fields, which is not the case when considering creeping faults.

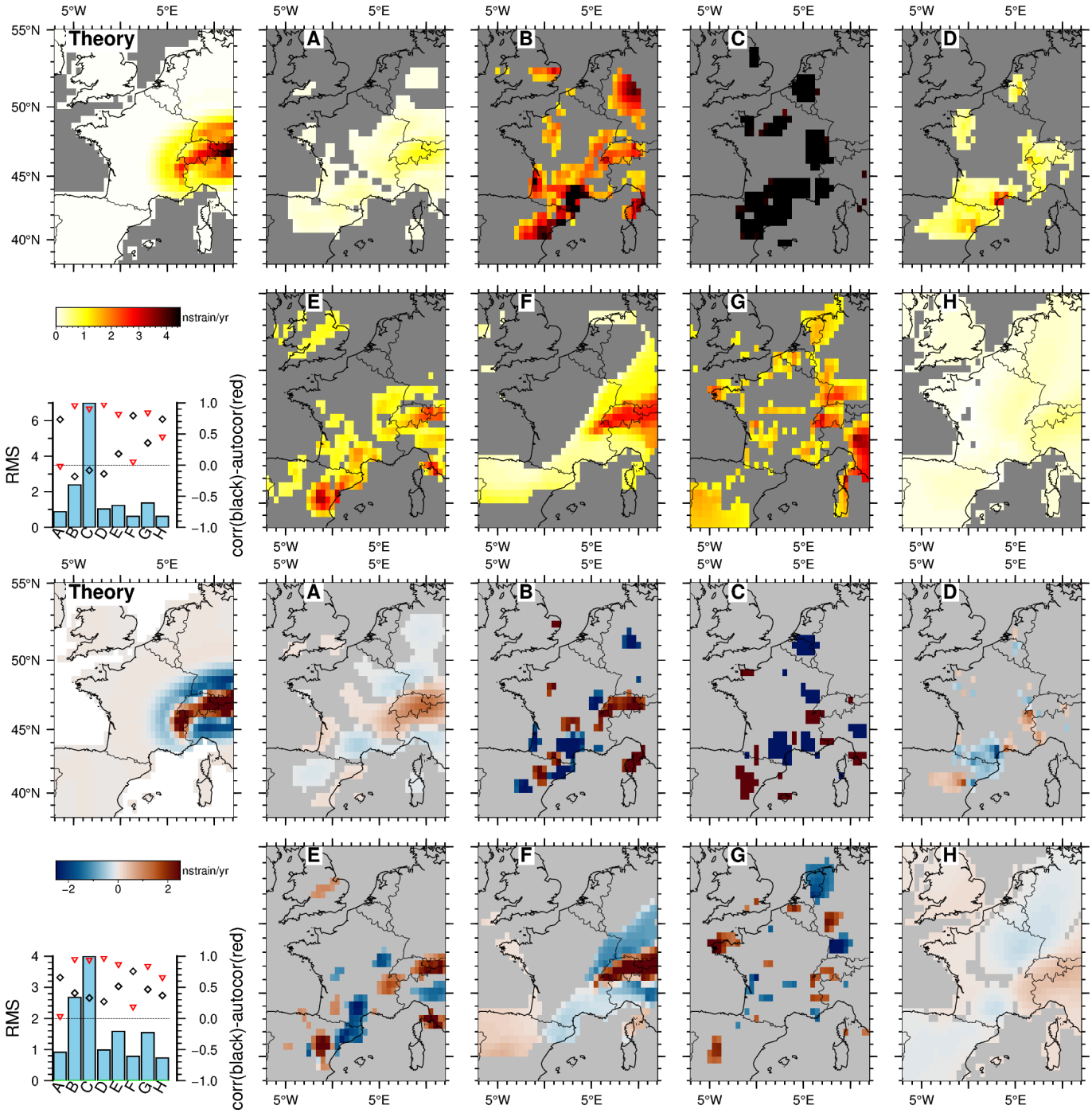

Figure 5 – Maps of theoretical (upper left panel) and retrieved (onshore only) I_2 (top) and divergence (bottom) for model 8 (Alpine GIA). Retrieved maps are masked based on the threshold values determined in section 4.1 and Table 3. Lower left graphs show computed statistics. Autocorrelation is computed with respect to retrieved values for model 3 (reference noise model).

The theoretical strain rates are higher for model 5, in which faults are creeping at 1 mm/yr, than for model 6, in which faults are locked at similar rate and produce deformation at larger spatial scales. I_2 is only partially recovered (score ∼50%) for model 6 by contribution A and not at all for model 5. Retrieved patterns of divergence and vorticity are far from the expected for all contributions (see profile view in Figure S22, Supporting Information). When deformation due to locked faults is superimposed to deformation coming from flexural processes (model 10 in supplementary Figures S12 to S15), the tectonic style associated to single faults is not recovered at all.

Overall, these results indicate that it is easier to recover large wavelength deformation signals than intense but localized deformation. This is a direct effect of the spatial filtering or averaging imposed by most methods to remove short-wavelength velocity noise. When noise is considered to perturb the observed velocity fields, it is impossible to recover strain rate patterns associated with 1 mm/yr locked or creeping faults given the network characteristics, the level of noise,

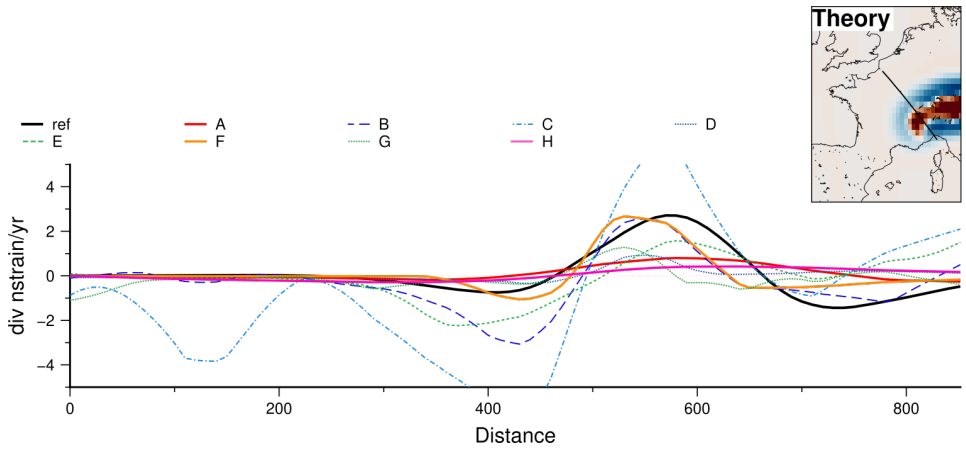

Figure 6 – Profile of expected (black bold line) versus retrieved divergence, along a profile line crossing the Alpine chain for model 8. Values originally sampled on a 0.5° grid have been interpolated. See Figure S16 (Supporting Information) for a profile sampling I_2 and the vorticity.

and the techniques selected in this exercise (see Section 5.1).

4.2.3 Do We See Rigid Block Motion?

We present retrieved maps of strain rate indicators for the Eulerian block model 7 in Figure 8, masked based on the confidence thresholds determined for each contribution. Contributions A and H recover some patterns of the second invariant, but systematically overestimate I_2 by $\sim 0.5 \times 10^{-9}$/yr in the center of the blocks where it should be zero, in particular where blocks are small and affected by the deformation along their boundaries. Divergence is not correctly recovered by any contribution. Vorticity is the most relevant indicator associated with the expected motion since we are looking for Eulerian rotations. All contributions but D retrieve the vorticity pattern with correlation scores of about 50% or higher. Contributions F and H give the most interpretable results since they provide spatially continuous results due to their low confidence thresholds. For model 11, in which block motion is superimposed to flexure from Alpine GIA and Massif Central (Figure S21, Supporting Information), we get roughly the same conclusions.

5 Discussion and Conclusions

Given the current design of our benchmark exercise, several first-order conclusions can be drawn :

1. Some contributions deal with noisy velocity fields better than others, namely A, F, and H based on the Geostrain (*Goudarzi et al.*, 2015), B-Strain (*Pagani et al.*, 2021) and BSF (*Okazaki et al.*, 2021) methods, respectively. These contributions generally perform better than others in recovering strain rates by being less sensitive to noise, but they fail like the others in recovering signals associated with active faults. Note that Geostrain is designed to capture continuous velocity fields with no discontinuity. On the contrary, some methods that appear to be sensitive to noise (B, E) are able to recover strain rates associated with the Alpine GIA, although not significantly outside of noise level (Figures 5 and 6).
2. Given the modeled noise characteristics in the GNSS velocity fields and the imposed rules of the game, none of the players were able to retrieve the expected strain rates associated with locked or creeping faults slipping at rates that are already too high for mainland France (i.e., 0.3 or 1 mm/yr).
3. Similarly, all players are blind to the tiny deformation produced by a supposed hotspot under the Massif Central (maximum values of 2 nstrain/yr for divergence, 1.5 nstrain/yr for I_2, and horizontal velocities lower than 1 mm/yr, vertical velocities about twice lower than those observed for the Eifel hotspot (*Kreemer et al.*, 2020)).
4. Some contributions, mainly A, F and H, are able to retrieve the overall shape of the strain rate patterns associated with signals producing deformation on large wavelengths, like the Alpine GIA or rotating rigid blocks. However, the amplitude of the strain rate indicators is not always captured properly.

These conclusions tend to show that there is still a long way to go before being able to capture small-scale signals associated with active faults in mainland France. However, these results must be interpreted with caution, keeping in mind the very strict rules of the game that we imposed during this community exercise.

5.1 Limitations and Warnings

In order to ease the comparison between the contributions, we ask the players to choose a single parameterization for all their calculations. This demand favors methods that are self-adaptive, i.e., that adapt the calculation parameters to the signal-to-noise ratio (either fixed *a priori* or automatically adjusted to the data set). In contrast, by adjusting "by hand" the smoothing parameters in the contributions based on *Shen et al.* (2015) approach (which implies having some knowledge of the noise affecting the velocity field), we could probably obtain better results.

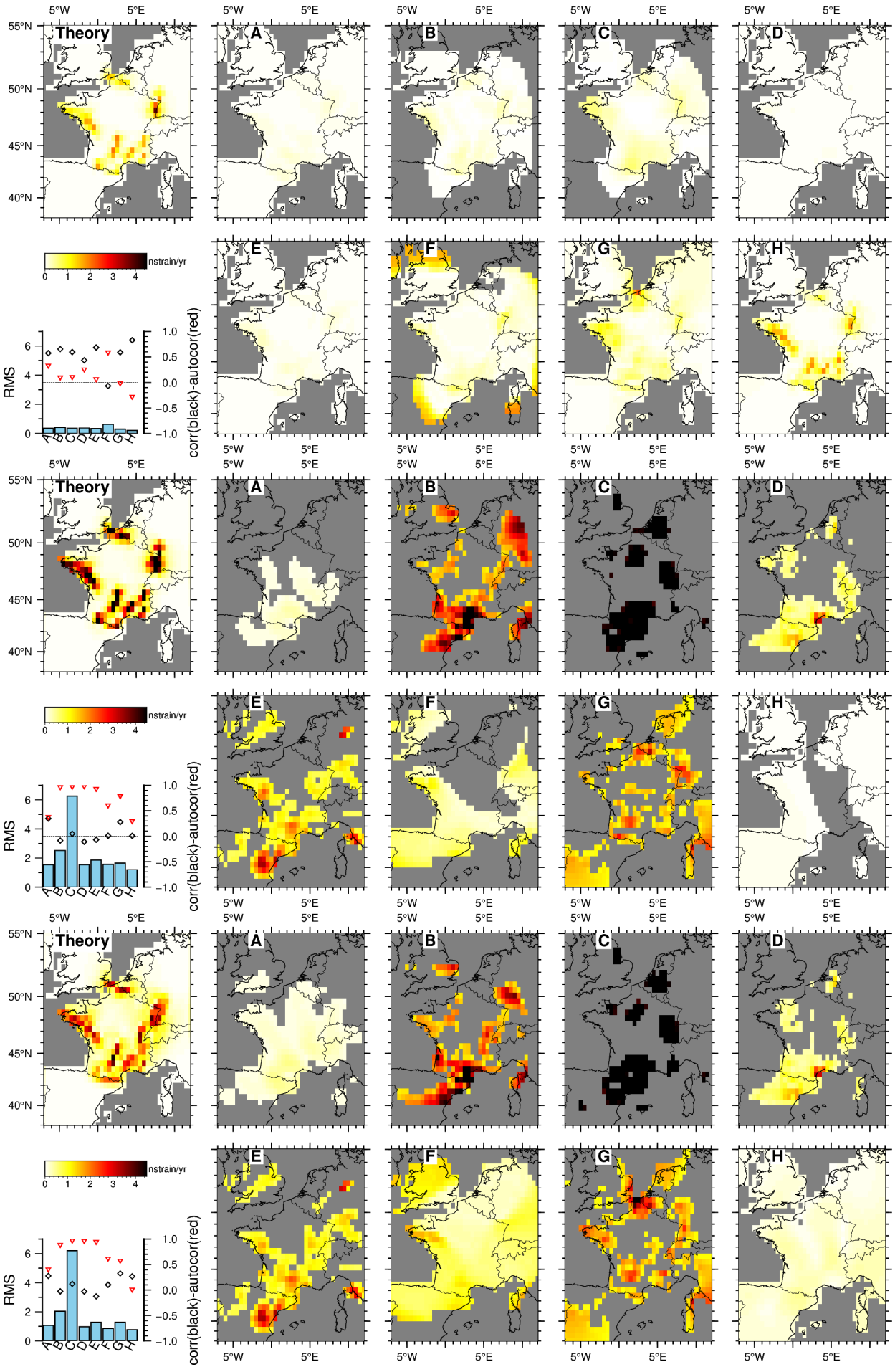

(**Figure 7**, caption on next page)

Figure 7 – Maps of theoretical (upper left panel) and retrieved (onshore only) I_2 for models 4 (creeping and no noise, top), 5 (creep and noise, middle), and 6 (locked and noise, bottom). Retrieved maps are masked based on the threshold values determined in section 4.1 and Table 3. Lower left graphs show computed standard statistics. Autocorrelation is computed with respect to retrieved values for model 3 (reference noise model).

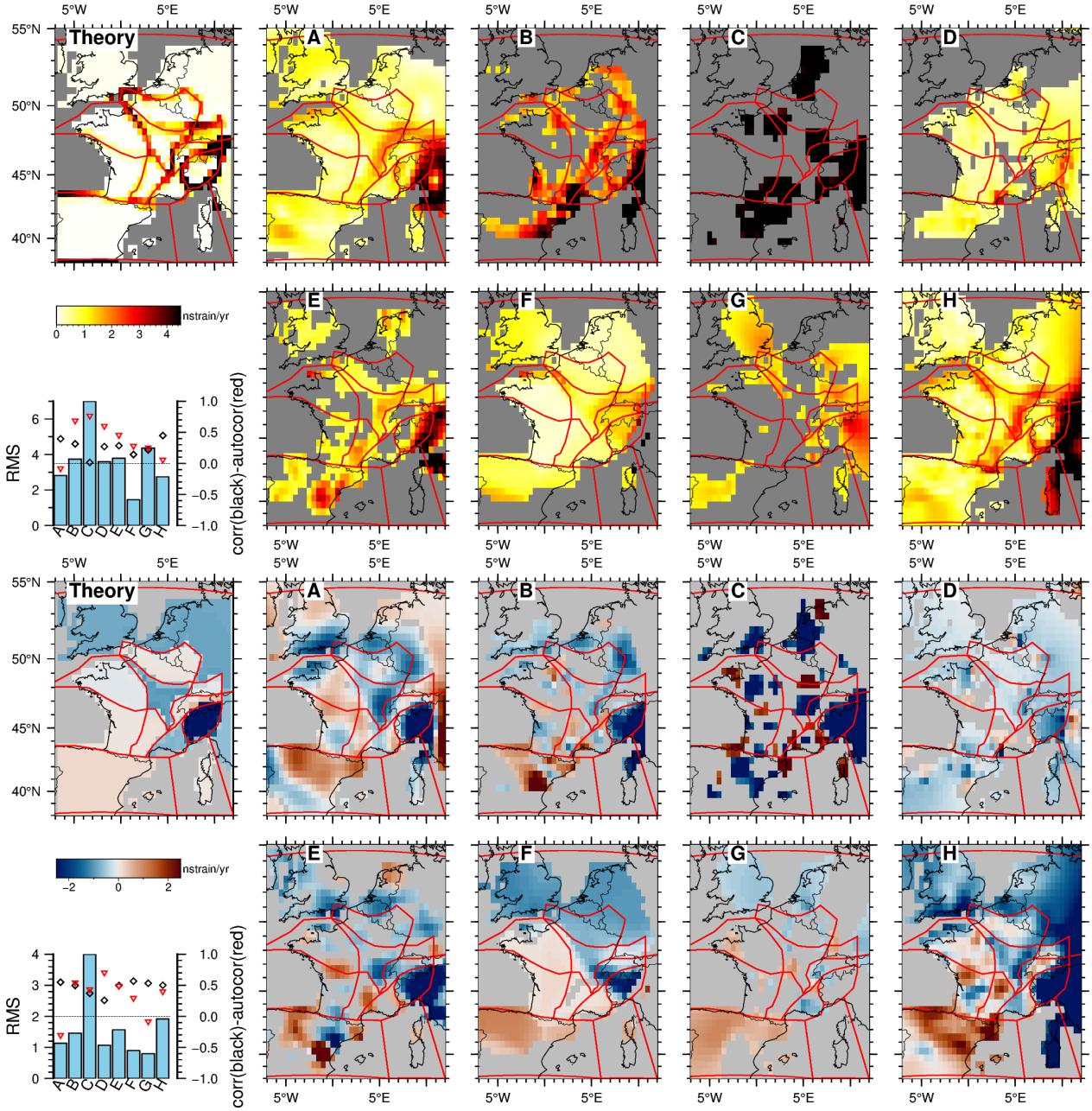

Figure 8 – Maps of theoretical (upper left panel) and retrieved (onshore only) I_2 (top) and vorticity (bottom) for model 7 (blocks and noise). Retrieved maps are masked based on the threshold values determined in section 4.1 and Table 3. Lower left graphs show computed standard statistics. Autocorrelation is computed with respect to retrieved values for model 3 (reference noise model). Red lines are the block boundaries.

We also ask the players to give only one solution for each model, while a common approach when dealing with real velocity fields is to produce several "realistic" or "preferred" strain rate calculations that give an idea of the method variability. In the specific case of contribution F, the player has to extract one single statistical indicator (here, the median) from the full probability density functions calculated as outputs of the BStrain code, which contains much more information on the plausible strain rate values. Other methods provide uncertainties associated with the strain rate tensor components that have not been analyzed here, although this could help interpret the results.

A restriction of our exercise is to use a velocity noise model with significant limitations, as presented in Section 4.1: the dispersion of the noise velocities may be too small compared to observations in mainland France, the noise velocities have no spatial correlation and low correlation between north-south and east-west components. The first point likely results in our strain

rate analyses being too optimistic, while the last two would likely improve our analyses if the correlations were included.

Based on the results obtained on the synthetic noise models and the confidence threshold values extracted from these (see Table 3), we should be safe in interpreting strain rates results (except when coming from the approach used without any tuning for the regional study, contribution C) if: divergence is higher than ± 1.5 nstrain/yr, $I_2 > 1.2$ nstrain/yr and $|\omega| > 0.4$ nstrain/yr (conservative values in Table 3). However, these confidence thresholds should be used with caution since they suggest that the best performing methods (i.e. contributions A, F, and H) should be able to see divergence higher than ± 0.07 nstrain/yr, $I_2 > 0.17$ nstrain/yr and $|\omega| > 0.033$ nstrain/yr, i.e., values much lower than the theoretical strain rates expected from fault models, which these methods fail to recover. The wavelength of the deformation signal and its position with respect to the network itself are also key parameters that should be considered together with these confidence thresholds that are too optimistic when considered alone.

5.2 The Strain Rate Game is not Over

Mainland France is not the easiest playground for geodesists looking for tectonic signals. By putting our effort on this benchmark exercise, we aim at pushing the boundaries of strain rate calculations toward very small strain rates expected in stable continental interiors.

Our main findings show that today, while we are probably able to recover correctly large-wavelength signals like GIA (although missing part of its amplitude), it is not reasonable to think that we can recover signals coming from loading on single active faults in strain rate calculations. However, this does not mean that GNSS-derived strain rates cannot give interesting information about the main local tectonic style: in particular, we should be able to see consistent block motions even associated with horizontal velocities of the order of the mm/yr. Strain rates computed for mainland France from real velocity fields with the strategy used in contribution E (*Masson et al.*, 2019a) are often found to be consistent in style with recent earthquakes, while this strategy is not outstanding in our benchmark exercise. Horizontal strain rates associated with Alpine GIA are among the signals that can be best estimated in our analyses (Figure 5). This is in agreement with studies using actual geodetic data in the Western Alps showing that GIA contributes significantly to observed vertical and horizontal velocities, and strain rates (e.g. *Nocquet*, 2012; *Masson et al.*, 2019a; *Sternai et al.*, 2019). Such results also have strong implications for active faults and seismic hazard, with a current debate regarding the potential impact of GIA fault activation (e.g. *Walpersdorf et al.*, 2018; *Grosset et al.*, 2023).

There is also room for improvement in the strain rate calculation methods or player strategies that could be adapted depending on the expected signal. The STIB method (*Masson et al.*, 2014, , contribution G) is performing better than most methods for velocity fields that are free of noise, but fails when noise is added, which could probably be improved. The BSF method (*Okazaki et al.*, 2021, , contribution H) is one of the methods that allows correct recovery of some geophysical strain rates but fails in recovering small-scale signals associated with faults. Some work is ongoing to improve the method, which currently does not take into account velocity uncertainties (*Ueda et al.*, 2024). B-Strain (contribution F based on (*Pagani et al.*, 2021)) is also one of the methods that perform relatively well. One limitation is that the inherent noise level of the data set is estimated without distinction between continuous and campaign mode measurements that are all considered together.

By gathering many researchers around this strain rate calculation problem in slowly deforming France, our scientific community is being pushed to tackle methodological issues and to propose solutions to reduce the noise associated with the surface velocity fields and to improve the spatial coverage in mainland France. The work started must continue in order to answer some strategic questions :

- Would we get better strain rate recovery if we had a denser velocity field with the same noise amount? Some locally denser velocity fields have been published recently (e.g. *Kreemer et al.*, 2020), suggesting room for improvement.
- Could we get better results by developing semi-permanent networks in low-density areas or around active faults, even if the uncertainties associated with such measurements are high and difficult to estimate?
- Would new velocities coming from dense but low-quality and recent networks, such as the collaborative Centipède low-cost network (*Bosser et al.*, 2024; *Ancelin et al.*, 2025), be sufficient to improve our calculations?
- Would it be enough to wait 10 more years to reduce the velocities uncertainties and get better strain rate estimates?
- Can we improve our calculations by taking into account spatial correlation in the GNSS position time series (*Costantino et al.*, 2023; *Gobron et al.*, 2024), or potentially in GNSS velocities?
- What if we finally get some reliable estimates of long-term velocity from InSAR (e.g. *Thollard et al.*, 2021; *Cheaib and Doin*, 2023; *Daout et al.*, 2023; *Lemrabet et al.*, 2023; *Meridi et al.*, 2025; *Viltres et al.*, 2025)?

Finally, this community benchmark exercise is certainly not over. The synthetic data sets and true models presented in section 3 are available online for other players to join the game, and for current players to refine their solutions (see Data Availability). Despite the limitations listed above, this study forms a solid foundation for moving on to the analysis of strain rate maps computed from real observed velocity fields over mainland France, and for integrating robust information

from geodesy into a new seismic hazard model for mainland France.

Acknowledgements

This work is part of the national Alceste (mainland France seismic hazard) project and is associated with the Epos-France infrastructure. It is supported by the "French Ministère de la transition écologique et de la cohésion des territoires", "Direction générale de la prévention des risques" (DGPR), convention #2201357292. It gathers many researchers involved in the national observation service RENAG (https://doi.org/10.15778/resif.rg), and has benefited from many feedback from the Epos-France community. We would like to thank the Tektonika editorial team, Corné Kreemer and Kathryn Materna for their advices and reviews, which helped in improving the manuscript.

Author contributions

M. Métois and **S. Mazzotti**: Conceptualization, Methodology, Supervision, Writing - Original draft, Funding Acquisition. **A. Periollat**: Methodology, Formal analysis, Investigation, Writing - Review & Editing. **All authors**: Formal analysis, Investigation, Writing - Review & Editing.

Data availability

The synthetic velocity fields (either raw or cleaned), the R-codes used to generate synthetic noise models and the strain rates computed for each methods are available on the EasyData repository: https://doi.org/10.57932/d194c240-858e-4838-90b5-536b2cbb28fd.

Competing interests

The authors declare no competing interests.

Peer review

This publication was peer-reviewed by two anonymous reviewers. The full peer-review report can be found here: Review Report.

Copyright notice

References

Anastasiou, D., A. Ganas, J. Legrand, C. Bruyninx, X. Papanikolaou, V. Tsironi, and V. Kapetanidis (2019), Tectonic Strain distribution over Europe from EPN data, in *Geophysical Research Abstracts*, vol. 21.

Ancelin, J., S. Ladet, and W. Heintz (2025), CentipedeRTK, un réseau pour la géolocalisation haute précision au service de l'environnement, *Journal of Interdisciplinary Methodologies and Issues in Sciences*, *12*, https://doi.org/10.46298/jimis.14252.

Antoine, S. L., Y. Klinger, A. Delorme, K. Wang, R. Bürgmann, and R. D. Gold (2021), Diffuse deformation and surface faulting distribution from submetric image correlation along the 2019 Ridgecrest, California, ruptures, *Bulletin of the Seismological Society of America*, *111*(5), 2275–2302, https://doi.org/10.1785/0120210036.

Barnhart, W. D., R. D. Gold, and J. Hollingsworth (2020), Localized fault-zone dilatancy and surface inelasticity of the 2019 Ridgecrest earthquakes, *Nature Geoscience*, *13*(10), 699–704, https://doi.org/10.1038/s41561-020-0628-8.

Baxter, S. C., S. Kedar, J. W. Parker, F. H. Webb, S. E. Owen, A. Sibthorpe, and D. Dong (2011), Limitations of strain estimation techniques from discrete deformation observations: LIMITATIONS OF STRAIN ESTIMATION, *Geophysical Research Letters*, *38*(1), https://doi.org/10.1029/2010gl046028.

Beauval, C., J. Marinière, H. Yepes, L. Audin, J.-M. Nocquet, A. Alvarado, S. Baize, J. Aguilar, J.-C. Singaucho, and H. Jomard (2018), A new seismic hazard model for Ecuador, *Bulletin of the Seismological Society of America*, *108*(3A), 1443–1464, https://doi.org/10.1785/0120170259.

Beavan, J., and J. Haines (2001), Contemporary horizontal velocity and strain rate fields of the Pacific-Australian plate boundary zone through New Zealand, *Journal of Geophysical Research*, *106*(B1), 741–770, https://doi.org/10.1029/2000jb900302.

Benoist, C., X. Collilieux, P. Rebischung, Z. Altamimi, O. Jamet, L. Métivier, K. Chanard, and L. Bel (2020), Accounting for spatiotemporal correlations of GNSS coordinate time series to estimate station velocities, *Journal of Geodynamics*, *135*(101693), 101,693, https://doi.org/10.1016/j.jog.2020.101693.

Bosser, P., J. Ancelin, M. Métois, L. Rolland, and M. Vidal (2024), Evaluation of tropospheric estimates from CentipedeRTK, a collaborative network of low-cost GNSS stations, *GPS Solutions*, *28*(4), 158, https://doi.org/10.1007/s10291-024-01699-3.

Cheaib, A., and M.-P. Doin (2023), Spatial unmixing of pixels for more accurate displacement time series obtained with a small baseline strategy: Application on France, in *IGARSS 2023 - 2023 IEEE International Geoscience and Remote Sensing Symposium*, pp. 7875–7877, IEEE, https://doi.org/10.1109/igarss52108.2023.10282268.

Chenel, F., G. Le Bliguet, T. Soubret, A. Rigo, P. Vernant, F. Perosanz, S. Durand, L. Morel, and J. Nicolas (2009), First results of the 2008 RESPYR GPS Campaign in the Pyrenees, *Gephys. Res. Abs*, *11*, 4535.

Cheng, G., and W. D. Barnhart (2021), Permanent co-seismic deformation of the 2013 Mw7.7 Baluchistan, Pakistan earthquake from high-resolution surface strain analysis, *Journal of Geophysical Research. Solid Earth*, *126*(3), e2020JB020,622, https://doi.org/10.1029/2020jb020622.

Cornou, C., J.-P. Ampuero, C. Aubert, L. Audin, S. Baize, J. Billant, F. Brenguier, M. Causse, M. Chlieh, A. Combey, M. de Michele, B. Delouis, A. Deschamps, M. Ferry, M. Foumelis, B. Froment, C. Gélis, R. Grandin, J.-R. Grasso, E. Hannouz, S. Hok, A. Jung, R. Jolivet, M. Langlais, P. Langlaude, C. Larroque, P. H. Leloup, K. Manchuel, L. Marconato, C. Maron, E. Mathot, E. Maufroy, D. Mercerat, M. Métois, E. Neyman, I. Pondaven, L. Provost, J. Régnier, J.-F. Ritz, D. Rivet, A. Schlupp, A. Sladen, C. Voisin, A. Walpersdorf, D. Wolynieck, P. Allemand, E. Beck, E. Bertrand, V. Bertrand, P. Briole, D. Brunel, O. Cavalié, J. Chèze, F. Courboulex, I. Douste-Bacqué, R. Dretzen, T. Giampietro, M. Godano, P. Grandjean, M. Grunberg, G. Guérin, S. Guillot, E. e. Haber, A. Hernandez, H. Jomard, C. Lasserre, C. Liang, I. Lior, X. Martin, D. Mata, M. Ménager, A. Mercier, A. Mordret, E. Oral, A. Paul, F. Peix, C. Péquégnat, M. Pernoud, C. Satriano, R. Sassi, M. Schaming, V. Sellier, C. Sira, A. Socquet, C. Sue, A. Trilla, M. Vallée, M. van den Ende, P. Vernant, B. Vial, and H. Weng (2020), Rapid response to the Mw 4.9 earthquake of November 11, 2019 in Le Teil, Lower Rhône Valley, France, *soumis à Compte Rendus Géoscience*, https://doi.org/10.31219/osf.io/3afs5.

Costantino, G., S. Giffard-Roisin, M. Radiguet, M. Dalla Mura, D. Marsan, and A. Socquet (2023), Multi-station deep learning on geodetic time series detects slow slip events in Cascadia, *Communications Earth & Environment*, *4*(1), 435, https://doi.org/10.1038/s43247-023-01107-7.

D'Agostino, N. (2014), Complete seismic release of tectonic strain and earthquake recurrence in the Apennines (Italy): D'AGOSTINO, *Geophysical Research Letters*, *41*(4), 1155–1162, https://doi.org/10.1002/2014gl059230.

Damon, A., S. Mazzotti, P. Vernant, R. Vachon, J. Grosset, F. Ego, and D. Baumont (2023), Impact of far-field glacially-induced stresses on fault stability in the eastern Paris Basin, *Tectonophysics*, *864*(230035), 230,035, https://doi.org/10.1016/j.tecto.2023.230035.

Daout, S., N. D'Agostino, E. Pathier, A. Socquet, J. Lavé, M.-P. Doin, M. Riesner, and L. Benedetti (2023), Along-strike variations of strain partitioning within the Apennines determined from large-scale multi-temporal InSAR analysis, *Tectonophysics*, *867*(230076), 230,076, https://doi.org/10.1016/j.tecto.2023.230076.

Donniol Jouve, B., A. Socquet, C. Beauval, V. P, L. Danciu, J. Donniol, and Bénédicte (2024), Consistency between the Strain Rate Model and ESHM20 Earthquake Rate Forecast in Europe: insights for seismic hazard, *EGUsphere*, *2024*, 1–32.

Déprez, A., A. Socquet, N. Cotte, and A. Walpersdorf (2018), Toward the generation of EPOS-GNSS products, in *9th General Assembly of WEGENER : on Earth deformation & the study of earthquakes using geodesy and geodynamics*, HAL open science.

Elliott, J., J. Fang, M. Lazecky, Y. Maghsoudi, Q. Ou, J. Payne, C. Rollins, D. Wang, A. Hooper, and T. Wright (2026), Deformation, strains and velocities for the Alpine Himalayan Belt from trans-continental Sentinel-1 InSAR & GNSS, *EarthArXiv*, https://doi.org/10.31223/x5gx6b.

Fernandes, R., C. Bruyninx, P. Crocker, J.-L. Menut, A. Socquet, M. Vergnolle, A. Avallone, M. Bos, S. Bruni, R. Cardoso, L. Carvalho, N. Cotte, N. D'Agostino, A. Deprez, F. Andras, F. Geraldes, G. Janex, A. Kenyeres, J. Legrand, K.-M. Ngo, M. Lidberg, T. Liwosz, J. Manteigueiro, A. Miglio, W. Soehne, S. Holger, S. Toth, J. Dousa, A. Ganas, V. Kapetanidis, and G. Batti (2022), A new European service to share GNSS Data and Products, *Annals of Geophysics*, *65*(3), DM317, https://doi.org/10.4401/ag-8776.

Gobron, K., P. Rebischung, K. Chanard, and Z. Altamimi (2024), Anatomy of the spatiotemporally correlated noise in GNSS station position time series, *Journal of Geodesy*, *98*(5), 34, https://doi.org/10.1007/s00190-024-01848-z.

Goudarzi, M. A., M. Cocard, and R. Santerre (2015), GeoStrain: An open source software for calculating crustal strain rates, *Computers & Geosciences*, *82*, 1–12, https://doi.org/10.1016/j.cageo.2015.05.007.

Grosset, J., S. Mazzotti, and P. Vernant (2023), Glacial-isostatic-adjustment strain rate–stress paradox in the Western Alps and impact on active faults and seismicity, *Solid Earth*, *14*(10), 1067–1081, https://doi.org/10.5194/se-14-1067-2023.

Haines, A. J., and W. E. Holt (1993), A procedure for obtaining the complete horizontal motions within zones of distributed deformation from the inversion of strain rate data, *Journal of Geophysical Research*, *98*(B7), 12,057–12,082, https://doi.org/10.1029/93jb00892.

Jenny, S., S. Goes, D. Giardini, and H.-G. Kahle (2004), Earthquake recurrence parameters from seismic and geodetic strain rates in the eastern Mediterranean, *Geophysical Journal International*, *157*(3), 1331–1347, https://doi.org/10.1111/j.1365-246x.2004.02261.x.

Jomard, H., E. M. Cushing, L. Palumbo, S. Baize, C. David, and T. Chartier (2017), Transposing an active fault database into a seismic hazard fault model for nuclear facilities – Part 1: Building a database of potentially active faults (BDFA) for metropolitan France, *Natural Hazards and Earth System Sciences*, *17*(9), 1573–1584, https://doi.org/10.5194/nhess-17-1573-2017.

Jouve, B. D., D. Marsan, A. Socquet, and C. Beauval (2024), Assessing the adequacy of earthquake catalog sampling for long-term seismicity in low-to-moderate seismic regions: A geodetic perspective, *Seismological Research Letters*, *95*(6), 3494–3506, https://doi.org/10.1785/0220240232.

Kreemer, C., J. Haines, W. E. Holt, G. Blewitt, and D. Lavallee (2000), On the determination of a global strain rate model, *Earth, Planets, and Space*, *52*(10), 765–770.

Kreemer, C., G. Blewitt, and P. M. Davis (2020), Geodetic evidence for a buoyant mantle plume beneath the Eifel volcanic area, NW Europe, *Geophysical Journal International*, *222*(2), 1316–1332, https://doi.org/10.1093/gji/ggaa227.

Lemrabet, L., M.-P. Doin, C. Lasserre, and P. Durand (2023), Referencing of continental-scale InSAR-derived velocity fields: Case study of the Eastern Tibetan plateau, *Journal of Geophysical Research. Solid Earth*, *128*(7), e2022JB026,251, https://doi.org/10.1029/2022jb026251.

Li, C., T. Li, J. Hollingsworth, Y. Zhang, L. Qian, and X. Shan (2023), Strain threshold for the formation of coseismic surface rupture, *Geophysical Research Letters*, *50*(16), e2023GL103,666, https://doi.org/10.1029/2023gl103666.

Manchuel, K., P. Traversa, D. Baumont, M. Cara, E. Nayman, and C. Durouchoux (2018), The French seismic CATalogue (FCAT-17), *Bulletin of Earthquake Engineering*, *16*(6), 2227–2251, https://doi.org/10.1007/s10518-017-0236-1.

Masson, C., S. Mazzotti, P. Vernant, and E. Doerflinger (2019a), Extracting small deformation beyond individual station precision from dense Global Navigation Satellite System (GNSS) networks in France and western Europe, *Solid Earth*, *10*(6), 1905–1920, https://doi.org/10.5194/se-10-1905-2019.

Masson, C., S. Mazzotti, and P. Vernant (2019b), Precision of continuous GPS velocities from statistical analysis of synthetic time series, *Solid Earth*, *10*(1), 329–342, https://doi.org/10.5194/se-10-329-2019.

Masson, F., P. Collard, J. Chéry, J. Ritz, E. Doerflinger, O. Bellier, D. Chardon, and M. Flouzat (2003), The VENICE project : A GPS network to monitor the deformation of western Provence and eastern Languedoc (southern France), in *EGS - AGU - EUG Joint Assembly*, p. 4482.

Masson, F., M. Lehujeur, Y. Ziegler, and C. Doubre (2014), Strain rate tensor in Iran from a new GPS velocity field, *Geophysical Journal International*, *197*(1), 10–21, https://doi.org/10.1093/gji/ggt509.

Mazzotti, S., L. J. Leonard, J. F. Cassidy, G. C. Rogers, and S. Halchuk (2011), Seismic hazard in western Canada from GPS strain rates versus earthquake catalog, *Journal of Geophysical Research*, *116*(B12), https://doi.org/10.1029/2011jb008213.

Meletti, C., W. Marzocchi, V. D'Amico, G. Lanzano, L. Luzi, F. Martinelli, B. Pace, A. Rovida, M. Taroni, F. Visini, and MPS Working Group (2021), The new Italian seismic hazard model (MPS19), *Annals of Geophysics*, *64*(1), https://doi.org/10.4401/ag-8579.

Meridi, A., M. Métois, C. Lasserre, M.-P. Doin, and P. Durand (2025), Active Straining of the Balkans Peninsula: insights from spatial geodesy (InSAR and GNSS), in *European Geosciences Union General Assembly 2025*, Copernicus GmbH, Vienna, Austria, https://doi.org/10.5194/egusphere-egu25-11094.

Mey, J., D. Scherler, A. D. Wickert, D. L. Egholm, M. Tesauro, T. F. Schildgen, and M. R. Strecker (2016), Glacial isostatic uplift of the European Alps, *Nature Communications*, *7*(1), 13,382, https://doi.org/10.1038/ncomms13382.

Métois, M., C. Lasserre, A. Méridi, M. Henriquet, and T. Bodin (2025), Bayesian estimation of surface strain rates in the Peri-Adriatic, Balkans and Aegean region from GNSS velocities, *Tektonika*, *3*, 82–98.

Nocquet, J.-M. (2012), Present-day kinematics of the Mediterranean: A comprehensive overview of GPS results, *Tectonophysics*, *579*, 220–242, https://doi.org/10.1016/j.tecto.2012.03.037.

Okada, Y. (1985), Surface deformation due to shear and tensile faults in a half-space, *Bulletin of the Seismological Society of America*, *75*(4), 1135–1154, https://doi.org/10.1785/bssa0750041135.

Okazaki, T. (2025), Program codes for crustal strain rate estimation using basis function expansion, https://doi.org/10.5281/ZENODO.16014772.

Okazaki, T., Y. Fukahata, and T. Nishimura (2021), Consistent estimation of strain-rate fields from GNSS velocity data using basis function expansion with ABIC, *Earth, Planets, and Space*, *73*(1), 1–22, https://doi.org/10.1186/s40623-021-01474-5.

Ou, Q., S. Daout, J. R. Weiss, L. Shen, M. Lazecký, T. J. Wright, and B. E. Parsons (2022), Large-scale interseismic strain mapping of the NE Tibetan plateau from sentinel-1 interferometry, *Journal of Geophysical Research. Solid Earth*, *127*(6), e2022JB024,176, https://doi.org/10.1029/2022jb024176.

Pagani, C., T. Bodin, M. Métois, and C. Lasserre (2021), Bayesian estimation of surface strain rates from global navigation satellite system measurements: Application to the southwestern United States, *Journal of Geophysical Research. Solid Earth*, *126*(6), e2021JB021,905, https://doi.org/10.1029/2021jb021905.

Petersen, M. D., A. M. Shumway, P. M. Powers, E. H. Field, M. P. Moschetti, K. S. Jaiswal, K. R. Milner, S. Rezaeian, A. D. Frankel, A. L. Llenos, A. J. Michael, J. M. Altekruse, S. K. Ahdi, K. B. Withers, C. S. Mueller, Y. Zeng, R. E. Chase, L. M. Salditch, N. Luco, K. S. Rukstales, J. A. Herrick, D. L. Girot, B. T. Aagaard, A. M. Bender, M. L. Blanpied, R. W. Briggs, O. S. Boyd, B. S. Clayton, C. B. DuRoss, E. L. Evans, P. J. Haeussler, A. E. Hatem, K. L. Haynie, E. H. Hearn, K. M. Johnson, Z. A. Kortum, N. S. Kwong, A. J. Makdisi, H. B. Mason, D. E. McNamara, D. F. McPhillips, P. G. Okubo, M. T. Page, F. F. Pollitz, J. L. Rubinstein, B. E. Shaw, Z.-K. Shen, B. R. Shiro, J. A. Smith, W. J. Stephenson, E. M. Thompson, J. A. Thompson Jobe, E. A. Wirth, and R. C. Witter (2024), The 2023 US 50-state National Seismic Hazard Model: Overview and implications, *Earthquake Spectra : The Professional Journal of the Earthquake Engineering Research Institute*, *40*(1), 5–88, https://doi.org/10.1177/87552930231215428.

Piña-Valdés, J., A. Socquet, C. Beauval, M.-P. Doin, N. D'Agostino, and Z.-K. Shen (2022), 3D GNSS velocity field sheds light on the deformation mechanisms in Europe: Effects of the vertical crustal motion on the distribution of seismicity, *Journal of Geophysical Research. Solid Earth*, *127*(6), e2021JB023,451, https://doi.org/10.1029/2021jb023451.

Pollitz, F. F., E. L. Evans, E. H. Field, A. E. Hatem, E. H. Hearn, K. Johnson, J. R. Murray, P. M. Powers, Z.-K. Shen, and C. Wespestad (2022), Western US deformation models for the 2023 update to the US National Seismic Hazard Model, *Seismological Society of America*, *93*(6), 3068–3086.

re3data.org (2022), RENAG-DC, https://doi.org/10.17616/R31NJN5L.

Rebischung, P., and K. Gobron (2024), Modeling random isotropic vector fields on the sphere: theory and application to the noise in GNSS station position time series, *Journal of Geodesy*, *98*(9), 79, https://doi.org/10.1007/s00190-024-01886-7.

RESIF (2017), RESIF-RENAG French national Geodetic Network, https://doi.org/10.15778/RESIF.RG.

Rigo, A., P. Vernant, K. L. Feigl, X. Goula, G. Khazaradze, J. Talaya, L. Morel, J. Nicolas, S. Baize, J. Chery, and M. Sylvander (2015), Present-day deformation of the Pyrenees revealed by GPS surveying and earthquake focal mechanisms until 2011, *Geophysical Journal International*, *201*(2), 947–964, https://doi.org/10.1093/gji/ggv052.

Sandwell, D., T. Becker, P. Bird, A. Freed, M. Hackl, W. Holt, B. Hooks, S. Kedar, C. Kreemer, and R. McCaffrey (2010), Comparison of 16 strain-rate maps of southern California, *SCEC Presentation*, *1*(5).

Santamaría, A. (2022), RENAG GNSS combined velocity field, https://doi.org/10.6096/5001.

Seguinot, J., S. Ivy-Ochs, G. Jouvet, M. Huss, M. Funk, and F. Preusser (2018), Modelling last glacial cycle ice dynamics in the Alps, *The Cryosphere*, *12*(10), 3265–3285, https://doi.org/10.5194/tc-12-3265-2018.

Shen, Z.-K., M. Wang, Y. Zeng, and F. Wang (2015), Optimal interpolation of spatially discretized geodetic data, *Bulletin of the Seismological Society of America*, *105*(4), 2117–2127, https://doi.org/10.1785/0120140247.

Sternai, P., C. Sue, L. Husson, E. Serpelloni, T. W. Becker, S. D. Willett, C. Faccenna, A. Di Giulio, G. Spada, L. Jolivet, P. Valla, C. Petit, J.-M. Nocquet, A. Walpersdorf, and S. Castelltort (2019), Present-day uplift of the European Alps: Evaluating mechanisms and models of their relative contributions, *Earth-Science Reviews*, *190*, 589–604, https://doi.org/10.1016/j.earscirev.2019.01.005.

Talaya, J., K. Feigl, A. Térmens, and I. Colomina (1999), Practical lessons from analysis of a GPS network designed to detect movements of 1mm/year in the eastern pyrenees, *Physics and Chemistry of the Earth Part A Solid Earth and Geodesy*, *24*(4), 355–359, https://doi.org/10.1016/s1464-1895(99)00041-1.

Thollard, F., D. Clesse, M.-P. Doin, J. Donadieu, P. Durand, R. Grandin, C. Lasserre, C. Laurent, E. Deschamps-Ostanciaux, E. Pathier, E. Pointal, C. Proy, and B. Specht (2021), FLATSIM: The ForM@Ter LArge-scale multi-Temporal Sentinel-1 InterferoMetry service, *Remote Sensing*, *13*(18), 3734, https://doi.org/10.3390/rs13183734.

Townend, J., and M. D. Zoback (2006), Stress, strain, and mountain building in central Japan: STRESS, STRAIN, AND MOUNTAIN BUILDING, *Journal of Geophysical Research*, *111*(B3), https://doi.org/10.1029/2005jb003759.

Ueda, T., A. Socquet, M. Métois, T. Okazaki, and T. Nishimura (2024), Objective estimation of strain rate field in and around the Balkans, in *Meeting of the Geodetic Society of Japan, Hiroshima*.

Vigny, C., J. Chéry, T. Duquesnoy, F. Jouanne, J. Ammann, M. Anzidei, J.-P. Avouac, F. Barlier, R. Bayer, P. Briole, E. Calais, F. Cotton, F. Duquenne, K. L. Feigl, G. Ferhat, M. Flouzat, J.-F. Gamond, A. Geiger, A. Harmel, M. Kasser, M. Laplanche, M. Le Pape, J. Martinod, G. Ménard, B. Meyer, J.-C. Ruegg, J.-M. Scheubel, O. Scotti, and G. Vidal (2002), GPS network monitors the Western Alps' deformation over a five-year period: 1993-1998, *Journal of Geodesy*, *76*(2), 63–76, https://doi.org/10.1007/s00190-001-0231-8.

Viltres, R., C. Doubre, M.-P. Doin, and F. Masson (2025), Aseismic creep and strain partitioning accommodating the Nubia-Eurasia oblique convergence in northern Africa from InSAR analysis, *Geology*, *53*(4), 349–354, https://doi.org/10.1130/g53117.1.

Walpersdorf, A., L. Pinget, P. Vernant, C. Sue, A. Deprez, and the RENAG team (2018), Does long-term GPS in the Western Alps finally confirm earthquake mechanisms?, *Tectonics*, *37*(10), 3721–3737, https://doi.org/10.1029/2018tc005054.

Wang, H., and T. J. Wright (2012), Satellite geodetic imaging reveals internal deformation of western Tibet: INTERNAL DEFORMATION OF WESTERN TIBET, *Geophysical Research Letters*, *39*(7), https://doi.org/10.1029/2012gl051222.

Wang, K. (2000), Stress–strain 'paradox', plate coupling, and forearc seismicity at the Cascadia and Nankai subduction zones, *Tectonophysics*, *319*(4), 321–338, https://doi.org/10.1016/s0040-1951(99)00301-7.

Ward, S. N. (1998), On the consistency of earthquake moment rates, geological fault data, and space geodetic strain: the United States, *Geophysical Journal International*, *134*(1), 172–186, https://doi.org/10.1046/j.1365-246x.1998.00556.x.

Wickert, A. D. (2016), Open-source modular solutions for flexural isostasy: gFlex v1.0, *Geoscientific Model Development*, *9*(3), 997–1017, https://doi.org/10.5194/gmd-9-997-2016.